Chain Packing Analysis of the Passivating Layer on Nanocrystalline Quantum Dot Surfaces

2 AUTHORS, INCLUDING:

Robert W Meulenberg
University of Maine

51 PUBLICATIONS **815** CITATIONS

Chain Packing Analysis of the Passivating Layer on Nanocrystalline Quantum Dot Surfaces

Robert W. Meulenberg and Geoffrey F. Strouse*

Department of Chemistry, University of California, Santa Barbara California 93106

Received: January 31, 2001; In Final Form: June 7, 2001

The organic passivant layer on nanomaterial surfaces has been examined by correlating the phase behavior of the passivant using attenuated total reflection infrared spectroscopy (ATR-IR), coupled with differential scanning calorimetry (DSC). The thermodynamic melting dynamics in the passivant layer supports the description of self-assembled monolayer-like interactions, with an initial constrained chain melting followed by modulation of the surface packing. Correlation of chain length with particle diameter and headgroup functionality suggests that in systems in which the radius of the particle is larger than the passivant layer thickness, chain−chain interactions dominate thermodynamic stabilities, with only a minimal contribution from headgroup stabilization of the passivating layer.

1. Introduction

Nanoscale materials in the size regime 1−100 nm (10−1000 Å) have long held promise for applications ranging from electronics to catalysis to nonlinear optoelectronic materials.[1] Materials (metals, semiconductors, or insulators) at the nanoscale exhibit bulk like crystallographic properties yet have physical properties governed by the particle size arising from the strong confinement of the charge carriers.[2] This class of semiconductor quantum dot (QD) materials can be readily prepared using lyothermal techniques producing narrow size distributions (5−8%) of materials that are surface-passivated by amphiphillic molecules and fully dispersible in organic solvents.[3,4] The unique physical properties and ease of processing these materials has resulted in a drive to harness the core-dependent properties, while the surface passivation layer has been largely ignored.

Typically, the surface layer consists of strong Lewis bases that act to thermodynamically stabilize the surface through a headgroup-surface interaction via coordination to the nanomaterial surface. The monolayer consists of organic moieties with long-chain functionalized alkanes, where the functionalities can be phosphines,[3] thiols,[5] or amines,[4] similar to a self-assembled monolayer (SAM), Langmuir−Blodgett (L−B) film, micelle, or liquid crystal. While SAMs represent surfaces with appended amphiphiles constrained in two-dimensions, the passivation on a quantum dot is constrained three-dimensionally. The constrained surfaces of these materials should exhibit a varied order/disorder behavior for the surface-passivated layer which correlates with passivant chain length, chain packing, and QD size. Recent efforts to understand the molecular level interactions and reactivity in nanoscale materials include small-molecule surface binding effects on photoluminescence,[6,7] NMR of the organic passivating layer,[8,9] varying of the capping layer moiety,[10−12] influence of the quantum dot shape,[13] and vibrational and thermotropic analysis of materials.[14−18] These studies indicate that the primary function of the capping moiety for the QD is minimization of particle agglomeration arising from Ostwald ripening, as well as passivation of the surface electronic states via surface reconstruction of dangling bonds at the solution/nanoparticle interface. Because of the large surface-to-volume ratios in these materials, the molecular level interactions of the passivant layer may also dominate particle−particle interactions in self-assembled three-dimensional structures. Furthermore, surface curvature effects may modulate the thermodynamics of chain packing at these surfaces.

Surface curvature effects play a substantial role in the importance of the passivant layer on a nanocrystal surface since the interdot interactions in three-dimensional assemblies are affected by the density of packing of the passivant layer at the surface of the nanocrystal. As the surface curvature increases, the packing density decreases due to an increase in free volume for the passivant chains. In SAM structures and metalomesogenic structures, where the surface is nominally flat, a two-step melting curve is observed for the organic phase,[19,20] due to limitation of both rotational and translational degrees of freedom for the tightly packed monolayer structures. Nuzzo et al. demonstrated a thermotropic transition in SAMs that has not been observed on nanomaterial surfaces arising from thermotropic activation of rotational degrees of freedom.[19] This low-temperature transition in crystalline gold SAM structures results in the ordering of the alkanethiol chain transformation from orthorhombic to a modified hexagonal "rotator" phase, coupled with a significant increase in gauche defect population of the polymethylene chains.[21] Such rotational transitions may also arise in nanomaterials where surface curvature effects may effect rotational, as well as translational degrees of freedom. In evaporatively assembled nanocrystals, surface curvature and the ratio of particle radius to chain length will influence the passivant layer packing and therefore its thermotropic behavior. Depending on this ratio, a 3-d assembly may be observed, in which dot−dot interactions exhibit interdot, single-chain, and chain-bundle interdigitation to minimize chain free volume at the surface of the nanomaterial.[14,16,18] MD calculations[22] confirmed the importance of intermaterial interactions and surface curvature effects in these materials.

To clearly separate the influence of surface curvature effects on surface packing in QDs, as well the as forces governing chain packing (i.e., chain interdigitation), correlation of thermodynamic data and local chain structure on the QD surface is required. To gain insight into the nature of chain packing and

* Corresponding author. E-mail: strouse@chem.ucsb.edu. Fax: 805-893-4120. Phone: 805-893-5326.

Nanocrystalline Quantum Dot Surfaces

J. Phys. Chem. B, Vol. 105, No. 31, 2001 **7439**

TABLE 1: Identification and Assignment of C—H and N—H Stretching Modes (cm⁻¹) as a Function of CdSe Quantum Dot Size (Å) at 298 K

vibrational modes[a]	n-HDA	26	41	55	65	90
asym NH_2 str	3332.1	3333.3	3331.9	3333.0	3333.6	—
asym CH_3 str (op); r_a^-	2961.7	2962.0 (w, sh)	2960.9 (sh)	—	2962.8 (vw, sh)	2960.3
asym CH_3 str (ip); r_b^-	2954.5	2955.2	2954.6	2955.7	2955.5	2955.5
antisym CH_2 str; d_α^-	2922.6	2924.0 (w, sh)	2930.2 (sh)	2924.5 (sh)	2931.3	2922.6
antisym CH_2 str; d^-	2914.9	2915.2	2916.0	2915.5	2914.0	2916.0
sym CH_3 str; r^+	2873.6	2872.9	2871.5	2873.5	2872.9	2873.8
sym CH_2 str; d_α^+	2860.9	2861.8	2857.3	2861.0	2859.6	—
sym CH_2 str; d^+	2851.1	2850.2	2848.8	2850.2	2848.2	2851.0

[a] str, stretching; sym, symmetric; ip, in-plane; op, out-of-plane; w, weak; vw, very weak; sh, shoulder.

melting phenomena in QDs, we have performed correlated temperature-dependent FTIR and DSC measurements on QD glassy thin films. By comparing these data with temperature-dependent pXRD and TEM measurements, we show that chain packing in CdSe nanoparticles is comprised of three limits when deposited as a film, with two- and three-dimensional effects being the extremes. This behavior is also reflected in QD solutions, suggesting that the packing behavior arises largely from single dot effects, rather than dot-dot interactions. We present thermodynamic data that illustrate the three regimes are governed by the ratio of passivant chain length to nanoparticle radius and give rise to changes in packing densities and chain conformations at the QD surface.

2. Experimental Section

2.1. Materials. CdSe QDs were synthesized by a modification of standard lyothermal methods using either tri-octylphospine/oxide (TOP/O) or *n*-hexadecylamine (HDA) as the growth solvent.[3,23] Recapping of the CdSe was accomplished by ligand exchange techniques and verified by FT-IR spectroscopy.[3,24] Crystallinity and size dispersity of the materials are monitored by absorption, pXRD, and TEM analysis. Typical size dispersites are 5—8%, depending on growth method.

2.2. Thermotropic Measurements. All thermal measurements were performed on thin glassy films in order to allow direct comparison of the thermotropic behavior.

2.2.1. ATR-FTIR Spectroscopy. QD samples were dispersed in hexane, deposited on a 4 × 80 mm ZnSe 45° HATR plate (Pike Technologies), and allowed to slowly evaporate. Temperature-dependent ATR-FTIR data were collected on a Perkin-Elmer Spectrum GX system from 650 to 4000 cm⁻¹ with a resolution of 2 cm⁻¹. Temperature control between 25 and 120 °C (±1 °C) was achieved using a manual temperature control (Pike Technologies) coupled to the HATR plate.

2.2.2. DSC Measurements. QD samples were dispersed in hexane, deposited on an Al crucible, and allowed to slowly evaporate. The weight was recorded within ±0.2 mg. DSC data were recorded on a Perkin-Elmer (DSC-7) instrument under N_2 between 25 and 120 °C (298—393 K) at a heating rate of 5 °C/min. Calorimetric data were recorded by fitting the area under the endotherm transitions. The DSC measurements are not background-subtracted in order to eliminate contributions from baseline filtering. Thermodynamic quantities are the average of multiple runs from several samples to minimize batch-to-batch anomalies. All the DSC traces exhibit an exothermic return consistent with reversible transitions. TGA/ DTA measurements indicate no mass loss in the temperature range studied and indicate that ~20% of the QD mass arises from the surface-passivating layer (depending on chain length).

2.2.3. Small-Angle Powder X-ray Diffraction. SAXS data were taken on a Philips X'PERT MPD diffractometer using Cu

TABLE 2: Identification and Assignment of C—H and N—H Stretching Modes (cm⁻¹) as a Function of Alkylamine ($NH_2(CH_2)_nCH_3$) Chain Length at 298 K

vibrational modes[a]	n = 15 (41 Å)[b]	n = 7 (55 Å)
asym NH_2 str	3331.9	3333.0
asym CH_3 str (op); r_a^-	2960.9 (sh)	2963.0 (w, sh)
asym CH_3 str (ip); r_b^-	2954.6	2956.2
antisym CH_2 str; d_α^-	2930.2 (sh)	-
antisym CH_2 str; d^-	2916.0	2923.8
sym CH_3 str; r^+	2871.5	2872.8
sym $CH2$ str; d_α^+	2857.3	-
sym CH_2 str; d^+	2848.8	2854.0

[a] str, stretching; sym, symmetric; ip, in-plane; op, out-of-plane; w, weak; sh, shoulder. [b] CdSe QD size.

Kα radiation ($\lambda = 1.5418$ Å). Temperature measurements were performed between 25 and 80 °C (± 1 °C).

2.3. Transmission Electron Microscopy. TEM analysis was obtained on a JEOL 2010 microscope operated at 200 kV in bright-field mode using Ni-backed holey carbon TEM grids (SPI) with the Formvar removed. Size and size distribution measurements were obtained on a statistical subset of QDs by manual calculation of the QD images obtained by digitizing the micrograph negatives.

3. Results

3.1. Room-Temperature Infrared Absorption. Complete assignments of the infrared transitions for various particle sizes, chain lengths, and headgroups in analogy to modes observed in crystalline *n*-alkanes and SAMs are exhaustively listed in Tables 1—4 and the Supplementary Tables 1 and 2.[15,25,26] Comparison of IR data for CdSe between 26 and 90 Å capped with HDA is presented in Tables 1 and 3. FT-IR comparisons of alkylamine chain lengths of 8 and 16 carbon units are given in Tables 2 and 4. Comparison of different CdSe capping ligands, HDA, HDT (hexadecylthiol), and TOP/O are given in Supplementary Tables 1 and 2. For clarity, only the 41 Å CdSe passivated with HDA is fully described in detail in the following sections.

3.1.1. High-Frequency Region (2800—3350 cm⁻¹). Infrared absorption data between 2800 and 3100 cm⁻¹ at 298 K are presented in Figure 1 and Table 1 for nanocrystalline CdSe—HDA between 26 Å and 90 Å (HDA is *n*-hexadecylamine ($NH_2(CH_2)_{15}CH_3$)). The infrared peaks between 2800 and 3100 cm⁻¹ in Figure 1 are assigned to contributions form the ν_{CH} stretching modes (d^+, d^-) for —CH_2 along the polymethylene alkylamine chains and to the end-methyl groups (—CH_3) (r^+, r^-). Complete assignments can be made for all the QD sizes, chain lengths, and chain headgroup as indicated in Tables 1, 2, and S1.

Close inspection of the 41 Å CdSe—HDA infrared data allows assignment of the asymmetric CH stretching mode (r^- mode), at 2955 cm⁻¹. Using second derivitatives, the r^- can be

7440 *J. Phys. Chem. B, Vol. 105, No. 31, 2001*

Meulenberg and Strouse

TABLE 3: Identification and Assignment of Low-Frequency Modes (720−1800 cm^{-1}) as a Function of CdSe Quantum Dot Size (Å) at 298 K

vibrational modes[a]	n-HDA	26	41	55	65	90
CH$_2$ rock; P$_1$	722	722	719	723	721	722
P$_3$	731	736	731	736	738	737
P$_7$	772	770	770	770	769	765
P$_9$	794	794	796	794	794	785
P$_{11}$	816	816	816	818	816	820
P$_{13}$	859	862	859	862	862	859
P$_{CH3}$	893	889	893	896	900	892
P$_x$	927	940	927	929	939	935
P$_x$	973	966	966	969	964	967
P$_x$	995	-	995	995	998	1001
C−C−C skeletal; S$_x$	1024	1024	1022	1024	1024	1024
S$_x$	1061	1063	1059	1063	1066	1069
S$_x$	1083	1084	1082	1083	1083	1083
S$_x$	1129	1128	1131	1127	1121	1123
S$_x$	1153	1151	1153	1153	1155	1155
CH$_2$ Wag; W$_x$	1174	1173	-	1185	1173	1171
CH$_2$ Twist; T$_x$	1192	1194	1190	1192	1194	1194
W$_x$	1213	1212	1213	1213	1215	1217
T$_x$	1236	1235	1235	1237	1233	1230
W$_x$	1255	1255	-	1255	1255	1251
T$_x$	1264	1264	1264	1264	1265	1266
W$_x$	1279	1277	1276	1278	1280	1278
T$_x$	1301	1301	1301	1300	1300	1302
W$_x$	1315	1315	1315	1315	1315	1316
T$_x$	1330	1327	-	1327	1324	1329
W$_x$	1344	1344	1346	1344	1344	1346
CH$_3$ sym def, bend	1382	1381	1378	1381	1379	1381
P$_1$, ovt[b]	1439	1439	1437	1437	1439	1443
CH$_2$ def, scissor, δ	1471	1468	1463	1468	1467	1468
			1471			

[a] def, deformation; ovt, overtone; sym, symmetric; ip, in-plane. [b] First overtone of the fundamental P$_1$ should occur at ∼1440 cm^{-1}.

TABLE 4: Identification and Assignment of Low-Frequency Modes (720−1800 cm^{-1}) as a Function of Alkylamine (NH$_2$(CH$_2$)$_n$CH$_3$) Chain Length at 298 K

vibrational modes[a]	n = 15 (41 Å)[b]	n = 7 (55 Å)
CH$_2$ rock; P$_1$	719	723
P$_3$	731	738
P$_7$	770	764
P$_9$	796	−
P$_{11}$	816	804
P$_{13}$	859	836
P$_{CH3}$	893	889
P$_x$	927	945
P$_x$	966	970
P$_x$	995	−
C−C−C skeletal; S$_x$	1022	1024
S$_x$	1059	1055
S$_x$	1082	1083
S$_x$	1131	−
S$_x$	1153	1148
CH$_2$ Wag; W$_x$	−	−
CH$_2$ Twist; T$_x$	1190	1183
W$_x$	1213	1216
T$_x$	1235	1233
W$_x$	−	1256
T$_x$	1264	1268
W$_x$	1276	−
T$_x$	1301	1302
W$_x$	1315	−
T$_x$	−	1325
W$_x$	1346	1344
CH$_3$ sym def, bend	1378	1378
P$_{1\ ovt}$[c]	1437	1438
CH$_2$ def, scissor, δ	1463	1475
	1471	

[a] def, deformation; ovt, overtone; sym, symmetric; ip, in-plane. [b] CdSe QD size. [c] First overtone of the fundamental P1 should occur at ∼1440 cm^{-1}.
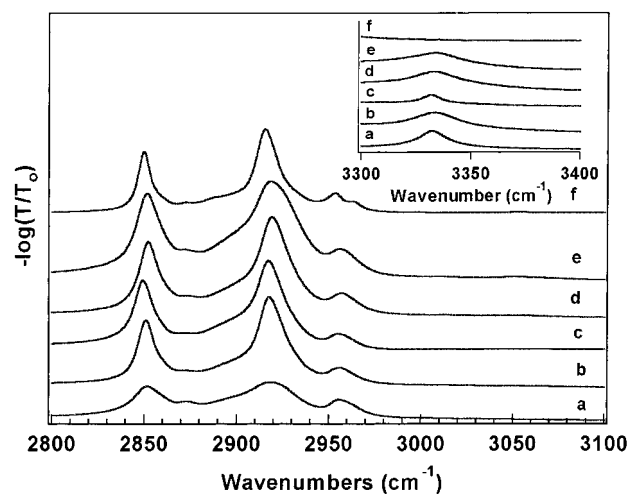
deconvoluted into contributions from the r$_b^-$ and r$_a^-$ modes at 2955 and 2960 cm^{-1}, respectively. The splitting of the asymmetric peak arises from the loss of C_3 symmetry of the alkylamine chain when it is covalently bonded to the QD surface, in analogy to what is seen in SAMs.[26] The small degree of splitting for the r$^-$ modes suggests hindered chain rotations about the long axis of the alkylamine ligand. The symmetric CH stretching mode (r$^+$) for 41 Å CdSe−HDA can be assigned at 2872 cm^{-1}. It is interesting to note that there is no evidence for the Fermi resonance band, which is observed for SAMs. This may possibly arise from symmetry-breaking along the chain due to chain tilt angles on the surface. Assignment of the −CH$_2$ ν_{CH} symmetric (d$^+$) and antisymmetric (d$^-$) stretching modes in the infrared absorption spectrum for the 41 Å CdSe−HDA occurs at 2848 and 2916 cm^{-1}, respectively. Second-derivative spectra reveal two additional peaks occurring at 2930 and 2857 cm^{-1}, which can be assigned to the symmetric and antisymmetric CH stretching modes of the CH$_2$ group closest to the headgroup (i.e., α-CH$_2$).[27] In the inset in Figure 1, the band at ∼3331 cm^{-1} most likely arises from the N−H asymmetric stretch. The shift in the N−H mode from ∼3370 cm^{-1}, typically observed in primary amines, is consistent with the weakening of the N−H bond upon covalent bonding to the QD surface. Shifts up to 60 cm^{-1} for the N−H mode have been observed when complexed to inorganic coordination compounds.[28] It is interesting to note in Figure 1 that at the largest QD sizes, there is a loss of ν_{NH}, possibly due to alkylamine/ surface interactions, implying that, in this size regime, the Cd−N molecular interaction changes.

3.1.2. Low-Frequency Region (600−1800 cm^{-1}). Figure 2b shows infrared absorbance spectra in the low-frequency region for CdSe−HDA. The spectra are presented as a function of QD

Figure 1. ATR−IR absorbance from 2800 to 3100 cm^{-1} of (a) n-HDA and (b) 26, (c) 41, (d) 45, (e) 65, and (f) 90 Å CdSe−HDA QD films at room temperature. Inset: Region from 3300 to 3400 cm^{-1} showing size dependence of the N−H stretch.

size, ranging from 26 to 90 Å, with n-HDA as a reference. The assignments are listed in Table 3. Complete assignments for all QD sizes, chain lengths, and chain headgroup are presented in Tables 3, 4, and S2.

The characteristic modes between 1450 and 1475 cm^{-1} are related to the −CH$_2$ and −CH$_3$ deformation modes. For a 41 Å CdSe QD, there are two contributions to these peaks. The strong band at ∼1463 cm^{-1} is from the in plane −CH$_3$ asymmetric deformation (α$_{ip}$), and the peak at ∼1471 cm^{-1} is due to the CH$_2$ deformation (δ).
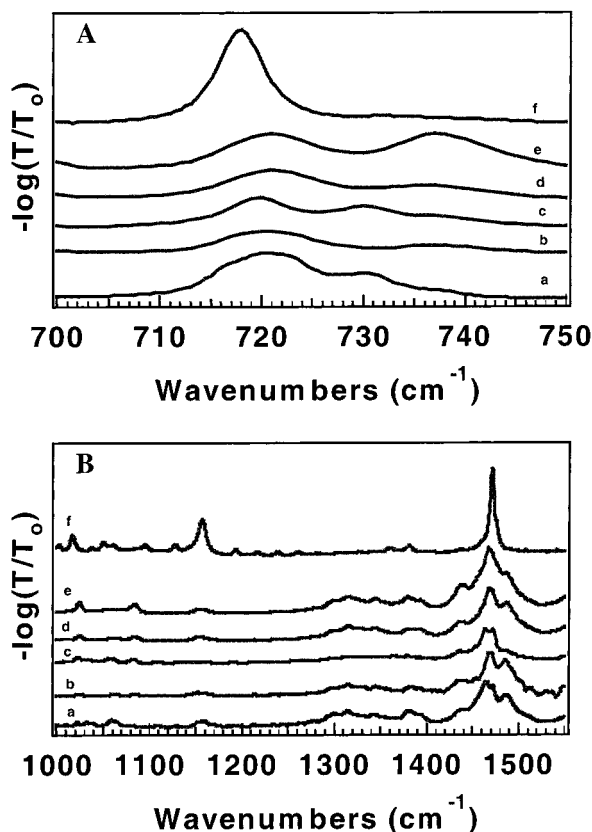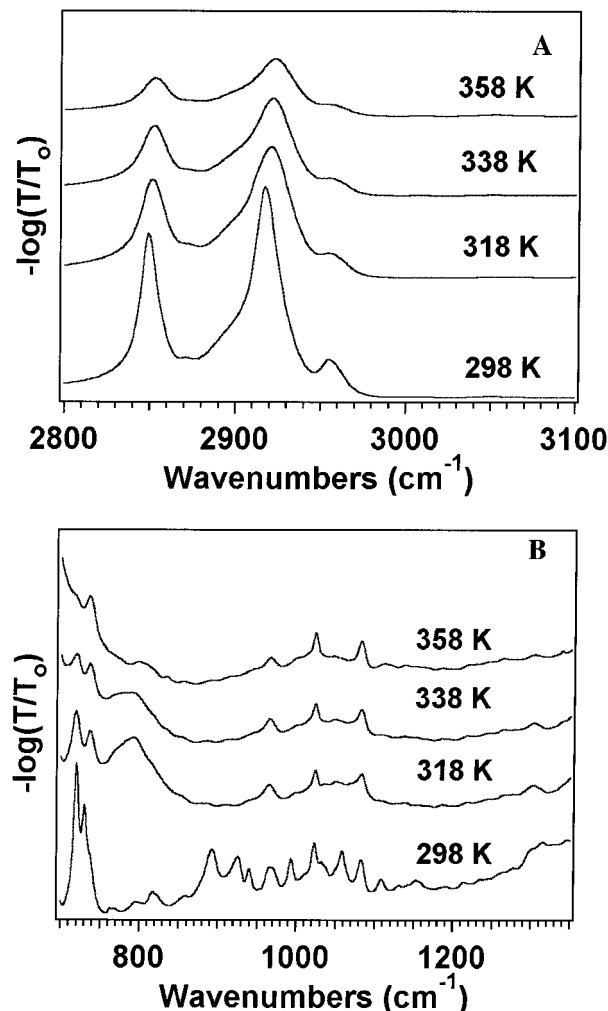
Figure 2. ATR−IR absorbance from (A) 700−750 cm^{-1} and (B) 1000−1550 cm^{-1} of (a) *n*-HDA and (b) 26, (c) 41, (d) 45, (e) 65, and (f) 90 Å CdSe−HDA QD films at room temperature.

The peak at ∼1378 cm^{-1} is assigned to the −CH$_3$ symmetric deformation (U). It is followed by a series of peaks between 1170 and 1350 cm^{-1} which are assigned to the progression series originating from the wagging (W$_x$) and twisting (T$_x$) vibrations of the methylene groups. The lack of the characteristic infrared signature for the end-gauche defect (∼1341 cm^{-1}) in QDs suggests an all-trans conformation in the alkylamine chains on the QD surface.

The progression of C−C−C skeletal vibrational (S$_x$) modes is observed between 1020 and 1150 cm^{-1}, followed by a set of bands between 710 and 1000 cm^{-1} arising from the CH$_2$ rocking modes (P$_x$). No N−H wagging is evident in this region due to the small cross section with respect to the C−H skeletal modes in this region. The peak at ∼720 cm^{-1} is attributed to the head-band (P$_1$) of the −CH$_2$ asymmetric rocking mode progression series. This mode is sensitive to the packing of the chains on the surface of the QD and is modulated by the QD size as indicated in Table 3. The 41 Å QD splits into two peaks, indicative of orthorhombic packing, while the other size QDs exhibit a single 720 cm^{-1} peak consistent with monoclinic or triclinic packing. The set of peaks from 650 to 700 cm^{-1} occurs in all spectra and is assigned to N−H wagging modes.

3.2. Temperature-Dependent Infrared Data. *3.2.1. High-Frequency Region (2800−3350 cm^{-1}).* Temperature-dependent ATR−IR spectra between 2700 and 3100 cm^{-1} on 41 Å CdSe−HDA QD is shown in Figure 3a. The d$^+$ and d$^-$ modes shift to higher energy with increasing temperature, indicating an increase in gauche defect population arising from the onset of chain melting. Such behavior is observed in crystalline alkanes and self-assembled monolayer structures.[19,29] Upon cycling the temperature, the modes do not completely recover (Supplemental Figure S1); however, the original position is observed for the

Figure 3. ATR−IR absorbance from (A) 2800−3100 cm^{-1} and (B) 700−1350 cm^{-1} as a function of temperature for 41 Å CdSe−HDA QD films.

modes after several days at RT, suggesting a slow kinetic recovery. Similar data are obtained for other sized QDs.

3.2.2. Low-Frequency Region (600−1800 cm^{-1}). Temperature-dependent ATR-IR spectra between 700 and 1350 cm^{-1} on a 41 Å CdSe−HDA QD is shown in Figure 3b. Upon heating, the P$_1$ (∼720 cm^{-1}) peak loses intensity. The progression modes (P$_x$, S$_x$, W$_x$, T$_x$) lose intensity with increased temperature indicative of increased conformational disorder. At the highest temperatures (∼368 K), the appearance of the 1341 cm^{-1} mode indicates the presence of gauche defects in the chains, consistent with the observation of an increase in gauche conformer population for the higher frequency IR data in section 3.2.1.

3.3. Differential Scanning Calorimetry. All DSC traces show reversible endothermic transitions for the various CdSe−HDA QD materials (Supplemental Figure S2). The enthalpic data represent average values for multiple runs on several samples and is presented in Table 5.[40] The low-temperature (T$_m$) endothermic peak at 315 K, assigned to the melting (ΔH_m) of the alkylamine chain, is observed for all QD sizes and the free chain. For the larger QDs, a second endothermic transition (T$_c$) is observed between 343 and 363 K, which is attributed to a chain collapse transition (vide infra), ΔH_c. Similar data were seen for QDs passivated with shorter alkylamine (i.e., OA − octylamine) substituents. A thermodynamic trend between ΔH_m and QD size is observed and represented in Figure 4.

TABLE 5: Chain Melt (ΔH_m) and Chain Collapse (ΔH_c) Enthalpies as a Function of CdSe QD Size (Å)

CdSe−HDA[a]		
size (Å)	ΔH_m[b] (kJ mol^{-1})	ΔH_c (kJ mol^{-1})
0 (n-HDA)	8.6 ± 0.5	−
26	8.0	−
40	5.7	−
45	2.6	21.3
80	4.2	4.1
90	5.4	12.3

[a] Hexadecylamine. [b] ΔH values reported per alkyl chain.
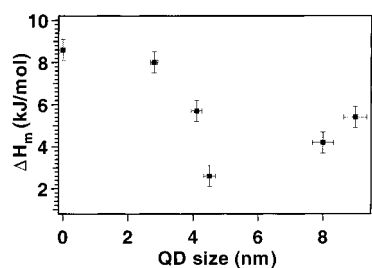
Figure 4. Melting enthalpies (ΔH_m) as a function of CdSe QD diameter passivated with HDA.

3.4. Structural Analysis. Temperature-dependent SAXS data are presented in Supporting Information, Supplemental Figure S3. The small-angle peaks, due to the superlattice of the QDs, lose all intensity between 318 and 358 K. The crystallographic reflections of the CdSe QD are not affected by temperature, showing no structural transformation in the temperature range studied.

Room-temperature TEM analysis of evaporated films are shown in Supplemental Figure S4. Statistical analysis of the TEM pattern indicates hexagonally packed structures with separation distances of ∼30 Å. This is consistent with intimate contact between the QDs and potentially interdigitation of either bundles or single chains, as previously suggested.[18]

4. Discussion

4.1. Molecular Orientation. Thermodynamic stabilization of the organic passivating layer on nanomaterials arises from the molecular level interactions of the chain packing at the organic/inorganic interface. Molecular packing can be described in terms of either chain−chain interactions providing crystallinity in the conformation or in terms of the surface packing density, which describes the packing lattice for the chains on the surface. Molecular packing is governed by a competition between the headgroup interactions (σ_{thiol} and A_{hs}, A_{tr}, A_{hh}) and the chain−chain packing interactions (δ_{SAM} and A_{att}, A_{conf}) (Figure 5). Such a model is analogous to micelle stabilization, self-assembled monolayers (SAMs), and Langmuir−Blodgett (L−B) structures, where a competition between entropic terms and enthalpic terms dictate the ratio of gauche conformers to all-trans conformers observed for the individual chains. In SAMs, a constrained all-trans geometry for the amphiphillic surface molecule is observed with increasing chain length, which is in the regime where enthalpic contributions dominate chain-packing thermodynamics.[30−33,41] As the density of packing decreases, there is an increase in entropic contributions to chain ordering at the molecular interface arising from an increase in rotational degrees of freedom. On a QD surface, surface curvature effects on packing densities complicate the competition between enthalpic and entropic terms. An all-trans conformation for the chains should be observed in cases where the
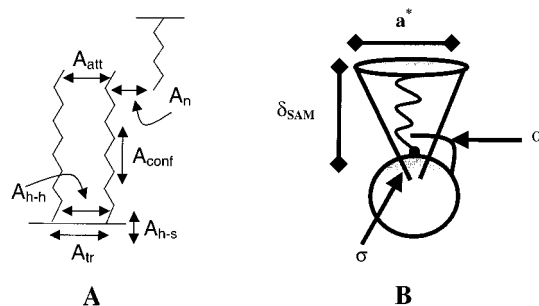
Figure 5. Schematic illustration of factors directing chain packing thermodynamics: (A) Free energy contributions to intra-, inter-, and neighboring van der Waals forces where A_{tr} is the translational entropy of the chains, A_{conf} is the conformational free energy of the chains, A_{att} is the attractive interaction between the chains, $A_{h−h}$ is the headgroup−headgroup interactions, $A_{h−s}$ is the headgroup-surface interactions, and A_n is a term that arises from any van der Waals interactions between chains of different dots (i.e., interdigitated chains). (B) Factors arising from the reduced dimensionality of QD surfaces where σ is the area per headgroup, $a*$ is the effective area per headgroup, α is the chain tilt, and δ_{SAM} is the passivant molecular density.

enthalpic terms dominate packing, particularly in the regime where chain length can compensate for surface curvature. In other words, larger nanoparticles would exhibit an effective lower passivation density on the basis of surface destabilization resulting from the decrease of thermodynamic contribution from the headgroup binding event. Smaller nanoparticles would have competing contributions from headgroup and chain−chain interactions as well as contributions from gauche (defect) conformers to maximize packing densities. Such effects have been observed for Au nanoparticles where the contribution of surface curvature leads to enhanced contributions of stabilization arising from headgroup interaction with the surface (A_{hs}) as the enthalpic stabilization from chain−chain interactions (A_{conf}) decrease with a decreases in Au particle radii.[34,35]

In an evaporatively assembled film of QDs, there are two limiting regimes for stabilization of the passivant layer: (a) single dot effects where the chain interactions are governed by A_{hs} and A_{att} and (b) dot−dot interactions where chain interactions arising from interdigitation and bundling contribute to the thermodynamic packing stability. Within these limiting cases, the interaction of the chains and the surface will be modulated by the ratio of the passivant chain length and the QD radius. Analysis of ATR-IR data in CdSe−HDA QD samples for the d$^+$, d$^−$ and r$^+$, r$^−$ modes (∼3000 cm^{-1}) and the gauche defect region (1300−1400 cm^{-1}) provides insight into the packing conformation of the alkylamine chains assembled at the QD/solution interface. For the ATR-IR data in Table 1 and Table 2, the d$^+$ and d$^−$ modes are observed between 2848 and 2850 and 2914−2916 cm^{-1}, consistent with an assignment of a predominantly all-trans packing arrangement at the surface of the CdSe QDs. As the QD size increases, a shift in the 2850 cm^{-1} mode to lower frequency and the 2915 cm^{-1} mode indicates an enhanced degree of crystallinity in the packing conformation. This is further supported by the increased contribution of T$_x$ and W$_x$ progressions for the 90 Å CdSe−HDA sample. For the HDA passivated materials, the degree of crystallinity is higher than that in the octylamine or solvated samples as seen in the shift of the d$^+$ and d$^−$ modes and loss of the twist and wag progressions, due to an increase in gauche conformer population in the 1300 cm^{-1} region.[26] Comparison of the vibrational data for solutions and films of QDs suggests that these nanoassemblies can be readily described in terms of single dot interactions for the chain−chain packing and governed largely by the surface curvature and length of the passivating

Nanocrystalline Quantum Dot Surfaces

J. Phys. Chem. B, Vol. 105, No. 31, 2001 **7443**

layer. The interdigitation or bundling of the chains may exist in these systems with evidence from TEM and SAXS data (Supp Figures 3 and 4) but may not contribute significantly to the phase behavior of the quantum dots based upon single particle interactions.

The influence of surface curvature is apparent in the lattice packing of the individual amphiphillic molecules. As the surface curvature increases, the density of packing appears to decrease, resulting in an increase in the degrees of rotational freedom. Freedom of rotation in the chain gives rise to two observable packing motifs in the CdSe lattice: hexagonal and orthorhombic (commonly referred to as herringbone). The 1467 and 720 cm^{-1} chain packing modes (P$_1$ and δ) provide direct insight into the packing motiff on the surface of the QDs. A single peak at ~1470 and 720 cm^{-1} occurs for all QD sizes except for the 41 Å QD and *n*-HDA, implying that the unit cell is a hexagonal cell arising from rotational freedom in the chains. This packing motif is observed in SAMs and has been postulated in Au nanoparticles. The orthorhombic packing of the *n*-HDA is similar to the low-temperature phases seen in crystalline *n*-alkanes.[36] Surprisingly, for the 41 Å QD, two peaks (~1463 and 1471 cm^{-1} and ~719 and ~730 cm^{-1}) of comparable intensity are observed which indicate that the chains are in an orthorhombic arrangement. The observation of orthorhombic packing on the highly constrained 41 Å CdSe may arise from enhanced headgroup surface interactions or from surface reconstruction leading to tighter chain packing on the surface of the small QD.

The assigned packing motifs are further supported by the thermal data predictions for the orthorhombic and hexagonal lattice.[37] For hexagonal packing, a low-energy melting transition is observed, while QDs with an orthorhombic arrangement undergo two phase transitions: (a) an orthorhombic to hexagonal transition and (b) a chain melt transition. Figure 3b shows temperature-dependent ATR-IR data that indicate that for the 41 Å QD loss of the 720 and 1470 cm^{-1} mode, splitting occurs immediately upon heating due to a first order phase transition from orthorhombic to hexagonal. The lack of an observable transition in the DSC probably arises from the fact that the orthorhombic to hexagonal transitions occur at temperatures only a few degrees less than the melt transitions.[36,38] The differences in the packing geometries can be understood in terms of packing densities. The two-step constrained melting in the larger QDs suggests a greater packing density of the chains on the QD surface. This suggests that the headgroup/ surface interactions become negligible when the particle radius exceeds the chain length.

4.2. Molecular Tilt. As the surface curvature on a QD increases, the packing density decrease can be compensated by the tilt angle of the amphiphilic molecule. As observed in SAMs, an increase in tilt angle allows enthalpic stabilization of the surface as the entropic contributions are decreased for the total packing motif. For CdSe QDs with a C$_{16}$ chain, all QD sizes below 90 Å show a stretch at ~3330 cm^{-1} (inset Figure 1), which is assigned to the asymmetric NH$_2$ stretch. The integrated intensity for ν_{NH} decreases with increasing size until the particle reaches 90 Å and the mode loses complete intensity. This can be attributed to a chain tilt on the surface of the QD as illustrated in Figure 7. As the chain takes a configuration resembling that in Figure 7a, surface selection rules dictate a screening of vibrational modes parallel to the surface. This implies that μ_{NH2} is beginning to approach zero, hence the loss in intensity of the mode. Nuzzo and co-workers have made similar arguments with alkanethiols absorbed on ZnSe semiconductor surfaces.[41] Coupled
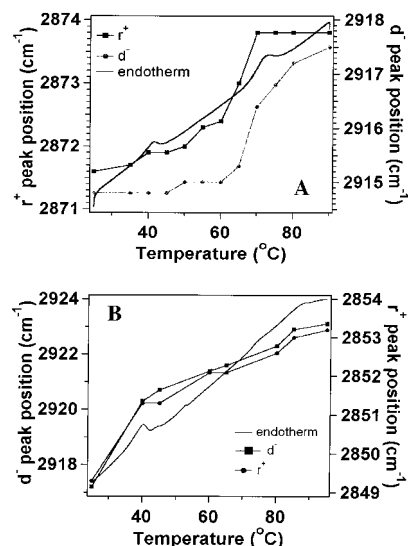
Figure 6. Thermotropic behavior of the d$^-$/ r$^+$ modes for (A) 90 and (B) 40 Å CdSe−HDA QD film. Note the strong correlation between the thermal behavior of the modes and the DSC endotherms.
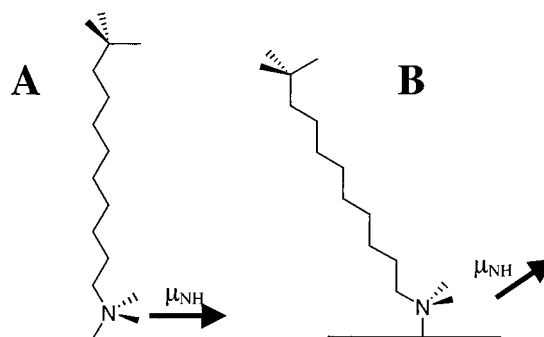
Figure 7. Schematic illustrations showing (A) chain tilt to maximize van der Waals forces and (B) possible chain orientation on small particles where packing density and constraints are less. Note the direction of the transition dipole moments.

with this decrease, a loss in intensity of ~20% is seen for the asymmetric CH$_2$ stretch (d$^-$) going from 26 to 90 Å, which is consistent with an increase in chain tilt for the largest QD implying that $\mu_{CH2} \to 0$. It is important to note that the cross section for methylene absorption is much higher than that for N−H absorption, explaining the difference in spectral behavior. Corroborating this assignment, the splitting of the r$^-$ mode into the in- and out-of-plane stretches shows a breaking of symmetry that can arise from tilting on the QD surface. It has also been shown that alkyl chains tilt to decrease their separation and increase their intermolecular van der Waals forces.[33] This behavior would result in better amphiphillic packing and increased crystallinity in the chains.

4.3. Thermodynamic Regimes. In the analysis of Au nanoparticles, it was demonstrated that strong surface/ headgroup dependence was observed for nanocrystals in which the passivant length (*l*) was smaller than the radius of the particle (*r*).[14,16] This suggests that there exists some thermodynamic minimum where the passivant free energy is minimized, and can be modeled in terms of three limiting cases:
(a) Case 1: *l* < *r* (2-d model − SAM model) QD surface appears flat with respect to the passivant.
(b) Case2: *l* > *r* (3-d model) QD surface curvature perturbs the molecular structure of the passivant.
(c) Case 3: *l* = *r* (special case−a very stable packing motif is predicted).

The three cases have different thermodynamic terms dominating packing, which in turn dominates chain tilt, chain melt, chain collapse, and chain surface interactions. For $l < r$ and $l > r$, either chain energy or chain entropy dictates the conformational free energy.[14,39] It is predicted that when $l = r$, the conformational free energy of the chains will be minimized. Murray et al. has suggested similar models for Au nanocrystals.[14] Thermal data coupled to IR analysis allow direct observation of these regimes. Thermodynamic melting transitions for $l > r$ is predicted[22] to melt at the same temperature as the free amphiphillic molecule, while melting in the $l < r$ regime is predicted to exhibit a two-step constrained melting curve, in which initial terminal gauche densities increase due to $-CH_3$ group rotational freedom occurring at the melt transition of the alkane, followed by an increase in intrachain gauche population, which can occur as high as 60 °C above that of the free amphiphillic molecule.[20]

In case 1, where $l < r$ ($2r > 41$ Å), the chain packing at room temperature is similar to SAMs, with minimal surface curvature effects for these materials. The chain packing motif is hexagonal and highly crystalline, with clearly resolved $(T_x + W_x)$ progressions for the 90 Å CdSe material. Furthermore, chain tilting appears in the 90 Å, consistent with packing at a pseudoplanar surface relative to the chain length. The chain melting on the surface exhibits two reversible phase transitions in the thermal and IR data. For the larger QD (Figure 6a), the r^+ mode is shifted to higher frequency upon heating, but the d^+ mode exhibits a delayed frequency shift, implying that the end-gauche and internal gauche conformers are not thermodynamically equivalent. This is reflected in large sized QD (i.e., radius is larger than chain length) normalized DSC endotherms where two transitions are seen, due to end-gauche conformers followed by complete chain collapse (Figure 6a). The first endothermic transition (T_m) occurs at ~315 K, with latent heats (ΔH_m) ranging between 3 (45 Å) and 5 (90 Å) kJ mol^{-1}, which substantially deviates from the free alkylamine melting transitions. A second transition (T_c) not witnessed in the free chain or $l > r$ regime occurs at higher temperatures, ranging between 70 and 75 °C (343–348 K), with latent heats (ΔH_c) that are highly size dependent. The trend for this size dependence may be due to packing constraints arising from chain tilt. Onset of the intrachain gauche defects is accompanied by increased conformational disorder, as evidenced by the loss of intensity from the twist and wag (T_x and W_x) progression series modes as a function of temperature. The melting progression and the small change in ΔH suggests that that the thermodynamic stabilization in these materials arises from chain–chain enthalpic contributions predominately.

For case 2, where $l > r$ ($l = 20.5$ nm, $2r < 41$ Å), surface curvature effects give rise to hexagonal packing and a lower crystallinity for the chains on the surface of the QD, as evidenced in the IR data. The loss of packing density is compensated in these materials by a minimization of chain tilt at the surface of the QD. Normalized thermal data comparison between *n*-HDA and CdSe–HDA supports the packing motif described above for the $l > r$ regime. For an *n*-HDA chain, there is one reversible solid–liquid phase transition corresponding to the melting of the alkyl chain. The melt is a correlated movement of all-trans chains to defect gauche states with latent heats of 8.6 kJ mol^{-1}. Upon ligation to a small CdSe particle, there still exists one reversible melting transition where the latent heats (ΔH_m) decrease, possibly due to the free energy gain from coordination of a dangling bond. The 26 and 40 Å CdSe show enthalpies of 8.0 and 5.7 kJ mol^{-1}, respectively, at ~42 °C
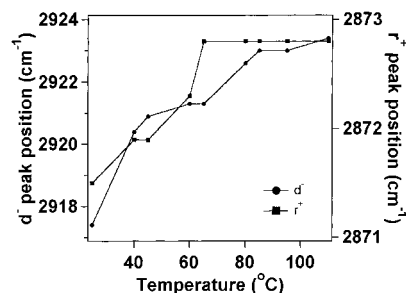
Figure 8. Thermotropic behavior of the d^-/r^+ modes for a 41 Å CdSe–HDA QD film.

(~315 K). The one-step melt represents a continuous melt of the chains above T_m due to lack of constraint arising from lattice packing. This implies a thermodynamic equivalence of the melting of the r^+ and d^- modes which is seen in the one DSC endotherm in Figure 6b. For $l > r$, chain tilting decreases to accommodate the lower packing density arising from surface curvature effects which decreases the methylene packing density by an increases in the effective area-per-headgroup, allowing greater rotational degrees of freedom.[14]

For case 3 ($l = r$), chain interactions and packing density constraints should exhibit the largest competition for control of the packing geometry at the inorganic/organic interface. In this regime, a C_{16} ligand ($l \approx 20.5$ Å) should produce the most stable packing for $a \approx 41$ Å QD. The IR data illustrate that the room temperature structure is crystalline with a herringbone (orthorhombic) packing motif. This packing motif gives rise to a highly constrained surface in which the packing density is maximized, by minimization of chain tilt, consistent with a case 2 thermodynamic regime for the room-temperature materials. Temperature-dependent IR data on the 41 Å CdSe (Figure 8) illustrate a linear shift in the d^- and r^+ modes to higher frequency, implying that both end-gauche and internal gauche conformers occur simultaneously upon heating, which is reminiscent of case 2 behavior. The thermal data suggest, however, that case 3 is closely related to case 1 behavior, as evidenced from the inflection point in the melting enthalpies in Figure 4. This suggests that changes in packing with temperature may result in a change in the appropriate thermodynamic regime as the headgroup/ surface interaction competes with the chain–chain interactions in the CdSe QD materials.

5. Conclusions

The packing of the alkylamine passivants on the surface of QD films is controlled by the competition of the free energy terms, A_{att}, A_{conf}, and A_{hs}. The dominance of these terms is influenced by surface curvature and the ratio of chain length to particle radius, giving rise to three distinct thermodynamic regimes. In the limiting cases, packing is controlled by A_{hs} (surface liagtion, with independent organic moieties) or dominated by A_{att} (chain–chain interactions). Competition between these two forces are intimately linked to the strength of the headgroup/surface interaction (Lewis basicity of the passivant), A_{conf} (chain-length), and QD radius (surface constraints). Stabilization of the QD surface is therefore fundamentally linked to the thermodynamics of stabilization of the passivant layer. This behavior arises from the size dependent nature of the three-dimensional constraint of the passivating layer on the QD surface.

Nanocrystalline Quantum Dot Surfaces

J. Phys. Chem. B, Vol. 105, No. 31, 2001 **7445**

Supporting Information Available: Figure S1 with thermotropic IR data. Figure S2 with DSC data. Figure S3 with temperature-dependent XRD data. Figure S4 with TEM micrograph. Tables S1 and S2 with IR assignments. This material is available free of charge via the Internet at http://pubs.acs.org.

References and Notes

(1) Steigerwald, M. L.; Brus, L. E. *Acc. Chem. Res.* **1990**, *23*, 183–188.

(2) Alivisatos, A. P. *J. Phys. Chem.* **1996**, *100*, 13226–13239.

(3) Murray, C. B.; Norris, D. J.; Bawendi, M. G. *J. Am. Chem. Soc.* **1993**, *115*, 8706–8715.

(4) Hines, M. A.; Guyot-Sionnest, P. *J. Phys. Chem. B* **1998**, *102*, 3655–3657.

(5) Kundu, M.; Khosravi, A. A.; Kulkarni, S. K.; Singh, P. *J. Mater. Sci.* **1997**, *32*, 245–258.

(6) Cordero, S. R.; Carson, P. J.; Estabrook, R. A.; Strouse, G. F.; Buratto, S. K. *J. Phys. Chem. B* **2000**, *104*, 12137–12142.

(7) Greenham, N. C.; Peng, X. G.; Alivisatos, A. P. *Phys. Rev. B—Condens. Matter* **1996**, *54*, 17628–17637.

(8) Sachleben, J. R.; Wooten, E. W.; Emsley, L.; Pines, A.; Colvin, V. L.; Alivisatos, A. P. *Chem. Phys. Lett.* **1992**, *198*, 431–436.

(9) Sachleben, J. R.; Colvin, V.; Emsley, L.; Wooten, E. W.; Alivisatos, A. P. *J. Phys. Chem. B* **1998**, *102*, 10117–10128.

(10) Noglik, H.; Pietro, W. J. *Chem. Mater.* **1995**, *7*, 1333–1336.

(11) Veinot, J. G. C.; Ginzburg, M.; Pietro, W. J. *Chem. Mater.* **1997**, *9*, 2117–2122.

(12) Veinot, J. G. C.; Galloro, J.; Pugliese, L.; Bell, V.; Pestrin, R.; Pietro, W. J. *Can. J. Chem.* **1998**, *76*, 1530–1539.

(13) Peng, X. G.; Manna, L.; Yang, W. D.; Wickham, J.; Scher, E.; Kadavanich, A.; Alivisatos, A. P. *Nature* **2000**, *404*, 59–61.

(14) Hostetler, M. J.; Stokes, J. J.; Murray, R. W. *Langmuir* **1996**, *12*, 3604–3612.

(15) Hostetler, M. J.; Wingate, J. E.; Zhong, C. J.; Harris, J. E.; Vachet, R. W.; Clark, M. R.; Londono, J. D.; Green, S. J.; Stokes, J. J.; Wignall, G. D.; Glish, G. L.; Porter, M. D.; Evans, N. D.; Murray, R. W. *Langmuir* **1998**, *14*, 17–30.

(16) Badia, A.; Cuccia, L.; Demers, L.; Morin, F.; Lennox, R. B. *J. Am. Chem. Soc.* **1997**, *119*, 2682–2692.

(17) Kim, B. S.; Avila, L.; Brus, L. E.; Herman, I. P. *Appl. Phys. Lett.* **2000**, *76*, 3715–3717.

(18) Prozorov, T.; Gedanken, A. *Adv. Mater.* **1998**, *10*, 532–535.

(19) Nuzzo, R. G.; Korenic, E. M.; Dubois, L. H. *J. Chem. Phys.* **1990**, *93*, 767–773.

(20) Bardeau, J. F.; Parikh, A. N.; Beers, J. D.; Swanson, B. I. *J. Phys. Chem. B* **2000**, *104*, 627–635.

(21) Ungar, G. *J. Phys. Chem.* **1983**, *87*, 689–695.

(22) Luedtke, W. D.; Landman, U. *J. Phys. Chem.* **1996**, *100*, 13323–13329.

(23) Khitrov, G. A.; Strouse, G. F. Manuscript in preparation.

(24) Cumberland, S. L.; Strouse, G. F. *Chem. Mater.*, submitted for publication.

(25) Snyder, R. G.; Schachtschneider, J. H. *Spectrochim. Acta* **1963**, *19*, 85–116.

(26) Parikh, A. N.; Gillmor, S. D.; Beers, J. D.; Beardmore, K. M.; Cutts, R. W.; Swanson, B. I. *J. Phys. Chem. B* **1999**, *103*, 2850–2861.

(27) MacPhail, R. A.; Strauss, H. L.; Snyder, R. G.; Elliger, C. A. *J. Phys. Chem.* **1982**, *86*, 5145–5150.

(28) Katari, J. E. B.; Colvin, V. L.; Alivisatos, A. P. *J. Phys. Chem.* **1994**, *98*, 4109–4117.

(29) Maroncelli, M.; Strauss, H. L.; Snyder, R. G. *J. Chem. Phys.* **1985**, *82*, 2811–2824.

(30) Laibinis, P. E.; Whitesides, G. M.; Allara, D. L.; Tao, Y. T.; Parikh, A. N.; Nuzzo, R. G. *J. Am. Chem. Soc.* **1991**, *113*, 7152–7167.

(31) Parikh, A. N.; Allara, D. L. *J. Chem. Phys.* **1992**, *96*, 927–945.

(32) Parikh, A. N.; Allara, D. L.; Azouz, I. B.; Rondelez, F. *J. Phys. Chem.* **1994**, *98*, 7577–7590.

(33) Ulman, A. *Chem. Rev.* **1996**, *96*, 1533–1554.

(34) Wilcoxon, J. P.; Martin, J. E.; Provencio, P. *Langmuir* **2000**, *16*, 9912–9920.

(35) Wilcoxon, J. P. Private communication, 2000.

(36) Nielsen, J. R.; Hathaway, C. E. *J. Mol. Spectrosc.* **1963**, *10*, 366–377.

(37) Kim, Y. S.; Strauss, H. L.; Snyder, R. G. *J. Phys. Chem.* **1989**, *93*, 7520–7526.

(38) Yoshida, H. *J. Thermal Anal. Calorimetry* **1999**, *57*, 679–685.

(39) Chaney, S. E.; Strouse, G. F. Unpublished results, 2000.

(40) The experimental ΔHs per gram are calculated using standard protocols. They are obtained by extrapolating a linear baseline to the trace and then fitting the area under the curve using this equation, $-A/Gkm$, where G and k are constants related to the DSC instrument, A is the peak area, and m is the sample mass. The reported ΔHs per mole are found using the following equation: $\Delta H_{reported} = (\Delta H_{exp}/0.22)MW$, where ΔH_{exp} is the raw experimental enthalpy which includes the total quantum dot mass and MW is the molecular weight of the passivant.

(41) Noble-Luginbuhl, A. R.; Nuzzo, R. G. *Langmuir* **2001**, *17*, 3937–3944.